

Dynamics of Asp23–Lys28 Salt-Bridge Formation in A β _{10–35} Monomers

Bogdan Tarus,[†] John E. Straub,^{*,†} and D. Thirumalai^{‡,§}

Contribution from the Department of Chemistry, Boston University, Boston, Massachusetts 02215, and Biophysics Program, Institute for Physical Sciences and Technology, and Department of Chemistry and Biochemistry, University of Maryland, College Park, Maryland 20742

Received July 8, 2006; E-mail: straub@bu.edu

Abstract: In the amyloid fibrils formed from long fragments of the amyloid β -protein (A β -protein), the monomers are arranged in parallel and lie perpendicular to the fibril axis. The structure of the monomers satisfies the amyloid self-organization principle; namely, the low free energy state of the monomer maximizes the number of intra- and interpeptide contacts and salt bridges. The formation of the intramolecular salt bridge between Asp(D)23 and Lys(K)28 ensures that unpaired charges are not buried in the low-dielectric interior. We have investigated, using all-atom molecular dynamics simulations in explicit water, whether the D23–K28 interaction forms spontaneously in the isolated A β _{10–35} monomer. To validate the simulation protocol, we show, using five independent trajectories spanning a total of 100 ns, that the pK_a values of the titratable groups are in good agreement with experimental measurements. The computed free energy disconnectivity graph shows that broadly the ensemble of compact random coil conformations can be clustered into four basins that are separated by free energy barriers ranging from 0.3 to 2.7 kcal/mol. There is significant residual structure in the conformation of the peptide in each of the basins. Due to the desolvation penalty, the structural motif with a stable turn involving the residues VGSN and a preformed D23–K28 contact is a minor component of the simulated structures. The extent of solvation of the peptides in the four basins varies greatly, which underscores the dynamical fluctuations in the monomer. Our results suggest that the early event in the oligomerization process must be the expulsion of discrete water molecules that facilitates the formation of interpeptide-interaction-driven stable structures with an intramolecular D23–K28 salt bridge and an intact VGSN turn.

1. Introduction

The amyloid β -protein (A β -protein) is the predominant protein component implicated in Alzheimer's disease (AD).¹ Recent studies have revealed that, besides the amyloid plaques with the characteristic cross β -pattern structure,² neurotoxicity can also be induced by apparently disordered soluble oligomers of the A β -protein.^{3–5} Thus, it is important to characterize, in molecular detail, not only the structures of the fibrils and oligomers but also the kinetics of their formation starting from the monomers. Although considerable progress has been made in the structural characterization of the fibril states of the

A β _{1–40}^{6,7} and shorter fragments using solid-state NMR⁸ and A β _{1–42}⁹ using mutagenesis and hydrogen-exchange NMR techniques, it has been difficult to determine the solution structures of monomers and oligomers at neutral pH. In this regard, molecular dynamics (MD) simulations have been useful in elucidating the structural fluctuations of the monomers and the interaction-driven formation of oligomers such as dimers and trimers.^{10–14}

The combination of experimental and computational studies by a number of groups^{7,9,15–21} suggests that formation of

[†] Boston University.

[‡] Institute for Physical Sciences and Technology, University of Maryland.

[§] Department of Chemistry and Biochemistry, University of Maryland.

- (1) Glenner, G. G.; Wong, C. W. *Biochem. Biophys. Res. Commun.* **1984**, *120*, 885–890.
- (2) Eanes, E. D.; Glenner, G. G. *J. Histochem. Cytochem.* **1968**, *16*, 673–677.
- (3) Lambert, M. P.; Barlow, A. K.; Chromy, B. A.; Edwards, C.; Freed, R.; Liosatos, M.; Morgan, T. E.; Rozovsky, I.; Trommer, B.; Viola, K. L.; Wals, P.; Zhang, C.; Finch, C. E.; Krafft, G. A.; Klein, W. L. *Proc. Natl. Acad. Sci. U.S.A.* **1998**, *95*, 6448–6453.
- (4) Walsh, D. M.; Hartley, D. M.; Kusumoto, Y.; Fezoui, Y.; Condron, M. M.; Lomakin, A.; Benedek, G. B.; Selkoe, D. J.; Teplow, D. B. *J. Biol. Chem.* **1999**, *274*, 25945–25952.
- (5) Hardy, J.; Selkoe, D. J. *Science* **2002**, *297*, 353–356.

- (6) Petkova, A. T.; Ishii, Y.; Balbach, J. J.; Antzutkin, O. N.; Leapman, R. D.; Delaglio, F.; Tycko, R. *Proc. Natl. Acad. Sci. U.S.A.* **2002**, *99*, 16742–16747.
- (7) Petkova, A. T.; Yau, W. M.; Tycko, R. *Biochemistry* **2006**, *45*, 498–512.
- (8) Tycko, R. *Curr. Opin. Struct. Biol.* **2004**, *14*, 96–103.
- (9) Luhrs, T.; Ritter, C.; Adrian, M.; Riek-Loher, D.; Bohrmann, B.; Dobeli, H.; Schubert, D.; Riek, R. *Proc. Natl. Acad. Sci. U.S.A.* **2005**, *102*, 17342–17347.
- (10) Klimov, D. K.; Thirumalai, D. *Structure* **2003**, *11*, 295–307.
- (11) Gsponer, J.; Haberthur, U.; Cafilisch, A. *Proc. Natl. Acad. Sci. U.S.A.* **2003**, *100*, 5154–5159.
- (12) Hwang, W.; Zhang, S.; Kamm, R. D.; Karplus, M. *Proc. Natl. Acad. Sci. U.S.A.* **2004**, *101*, 12916–12921.
- (13) Gnanakaran, S.; Nussinov, R.; Garcia, A. E. *J. Am. Chem. Soc.* **2006**, *128*, 2158–2159.
- (14) Jang, S.; Shin, S. *J. Phys. Chem. B* **2006**, *110*, 1955–1958.
- (15) Ma, B.; Nussinov, R. *Proc. Natl. Acad. Sci. U.S.A.* **2002**, *99*, 14126–14131.
- (16) George, A. R.; Howlett, D. R. *Biopolymers* **1999**, *50*, 733–741.
- (17) Chaney, M. O.; Webster, S. D.; Kuo, Y. M.; Roher, A. E. *Protein Eng.* **1998**, *11*, 761–767.

oligomers, protofilaments, and fibrils follow the principle of amyloid self-assembly (PASA). According to the PASA, the most favorable structures along the cascade of events that lead to amyloid fibrils starting from the monomers are those that maximize intra- and interpeptide hydrophobic interactions and salt bridges. The experimentally determined structures as well as oligomers that have been identified in simulations satisfy the PASA. For example, the antiparallel structures adopted by oligomers and fibrils of $A\beta_{16-22}$ ^{10,15} are in accord with the PASA. Explicit MD simulations of $A\beta_{16-22}$ ¹⁰ and $A\beta_{10-35}$ ²² show that, although the driving force for forming ordered structures is interpeptide hydrophobic interactions, favorable electrostatic interactions resulting in salt-bridge formation also play an important role.

The PASA, which emphasizes the role of side chains (and hence the sequence) in stabilizing oligomers and higher order structures, raises an important question concerning the role of charged residues in the assembly of long $A\beta$ -proteins such as $A\beta_{10-35}$ and $A\beta_{1-40}$. The solid-state NMR-based structures proposed by Tycko and co-workers^{6,7} for the fibrils of $A\beta_{1-40}$ include as a key structural element a bend involving residues 24–27, namely, VGSN. The structural motif with the VGSN turn and salt bridge between D23 and K28 ensures that isolated charges are not buried in the low-dielectric interior of the fibril. Such a structural motif when stacked in parallel leads to a fibril that satisfies the PASA.

Given that the structural precursors of the fibrils manifest themselves in soluble dynamically fluctuating oligomers, it is logical to postulate that the D23–K28 salt bridge must play an important role in the early events of self-association of long $A\beta$ -proteins. Molecular dynamics simulations of $A\beta_{9-40}$ fibrils suggest that partially solvated D23–K28 salt bridges appear to be arranged as in a one-dimensional ionic crystal.²¹ Luhrs et al.,⁹ using both NMR and mutagenesis experimental techniques, proposed a protofibril structure in which the D23–K28 salt bridge is not intramolecular but rather intermolecular. Motivated by these considerations, we investigate the extent to which the D23–K28 interaction forms in the $A\beta_{10-35}$ monomer using MD simulations of the protein in explicit water. The present study is important in addressing whether such preformed structures trigger oligomerization or whether interpeptide interactions are needed to induce the structures in monomers that can progress to form oligomers and higher order structures. Using extensive simulations and novel analysis of the data, we show that the formation of a stable structure with an intact D23–K28 salt bridge and the VGSN turn is highly improbable in the monomer. Our results suggest that overcoming the large barrier to desolvation of D23 and K28, which can only occur at finite peptide concentration, must be an early event in the formation of higher order structures.

2. Computational Models and Methods

2.1. Molecular Dynamics. The molecular dynamics simulation of the hydrated peptide was performed using the atomistic representation of both the solute and solvent. The potential energy of the system

includes the energy of the peptide in a vacuum and the explicit, pairwise, solute–solvent and solvent–solvent interactions. The program CHARMM,²³ with the PARAM22 all-atom force field²⁴ with the TIP3P three-site model for water,²⁵ was used to simulate the dynamics of the solvated peptide. The peptide was centered in a truncated octahedral cell that was carved from a larger preequilibrated cell of pure water. The size of the primary cell was set according to the minimum-image convention and periodic boundary conditions. The electrostatic energy was computed without truncation, using the particle mesh Ewald summation algorithm.²⁶ An FFT grid point spacing of 0.95 Å and a fifth-degree B-spline interpolation were used. The width of the Gaussian distribution in real space was 0.32 Å⁻¹. The van der Waals and real-space electrostatic interactions were smoothly shifted to zero at 10 Å. The list of the nonbonded interactions was truncated at 12 Å using an atom-based cutoff. The hydrogen atoms were constrained to the equilibrium bond length using the SHAKE algorithm.²⁷ The equations of motion were integrated using the leapfrog integrator with a step of 2 fs. The pressure was restrained to 1 atm using the Langevin piston algorithm,²⁸ and the temperature was maintained at 300 K using the Nosé–Hoover thermostat.²⁹ The NMR structure of the $A\beta_{10-35}$ -NH₂ protein (410 atoms)³⁰ was used for the initial coordinates. Starting from the same point in configuration space and from different points in velocity space, by using different values of the pseudorandom number generator, five different trajectories were generated. Four trajectories are 10 ns long, and the fifth was extended to 60 ns.

2.2. pK_a Calculations. The Macroscopic Electrostatics with Atomic Detail (MEAD)^{31,32} package was used to compute the pK_a values in a protein structure with multiple ionizable residues. We considered all eight titratable residues (Y10, E11, H13, H14, K16, E22, D23, and K28) for the $A\beta_{10-35}$ -protein. The dimension of the grid box was obtained by multiplying the maximum Cartesian dimension of the peptide structure by a factor of 2.0. A grid size of 1.0 Å was used in the first iteration step. A focusing second iteration step used a grid size of 0.25 Å, while the grid box was centered on the ionizable residue. A value of 80 was used as the dielectric constant for aqueous solution, while for the peptide structure two values of 4 and 20 were used. The pK_a values were computed for $A\beta_{10-35}$ structures separated by 10 ps in the simulated trajectories.

2.3. Analysis. A number of characteristics of the $A\beta_{10-35}$ -protein were computed using the five distinct trajectories (totaling 100 ns) in the explicit solvent model. We computed the distribution of the radius of gyration (R_g), root-mean-square fluctuations, and Lipari–Szabo orientational order parameter, S^2 .^{33,34} These quantities serve to characterize the global features of the $A\beta_{10-35}$ -protein. In addition, we also probed the microscopic fluctuations at the residue level to illustrate the role of water in inducing local structure formation. We also characterize the sampled macrostates, their free energies, and the barriers separating the macrostates.

- (18) Li, L.; Darden, T. A.; Bartolotti, L.; Kominos, D.; Pedersen, L. G. *Biophys. J.* **1999**, *76*, 2871–2888.
 (19) Lazo, N. D.; Downing, D. T. *Biochemistry* **1998**, *37*, 1731–1735.
 (20) Nelson, R.; Sawaya, M. R.; Balbirnie, M.; Madsen, A. O.; Riekel, C.; Grothe, R.; Eisenberg, D. *Nature (London)* **2005**, *435*, 773–778.
 (21) Buchete, N. V.; Tycko, R.; Hummer, G. *J. Mol. Biol.* **2005**, *353*, 804–821.
 (22) Han, W.; Wu, Y. D. *J. Am. Chem. Soc.* **2005**, *127*, 15408–15416.

- (23) Brooks, B. R.; Bruccoleri, R.; Olafson, B.; States, D.; Swaminathan, S.; Karplus, M. *J. Comput. Phys.* **1983**, *4*, 187–217.
 (24) MacKerell, A. D.; et al. *J. Phys. Chem. B* **1998**, *102*, 3586–3616.
 (25) Jorgensen, W. L.; Chandrasekhar, J.; Madura, J. D.; Impey, R. W.; Klein, M. L. *J. Chem. Physiol.* **1983**, *79*, 926–935.
 (26) Darden, T.; York, D.; Pedersen, L. *J. Chem. Phys.* **1993**, *98*, 10089–10092.
 (27) Ryckaert, J. P.; Ciccotti, G.; Berendsen, H. J. C. *J. Comput. Phys.* **1977**, *23*, 327–341.
 (28) Feller, S. E.; Zhang, Y. H.; Pastor, R. W.; Brooks, B. R. *J. Chem. Phys.* **1995**, *103*, 4613–4621.
 (29) Hoover, W. G. *Phys. Rev. A* **1985**, *31*, 1695–1697.
 (30) Zhang, S.; Iwata, K.; Lachenmann, M. J.; Peng, J. W.; Li, S.; Stimson, E. R.; Lu, Y.; Felix, A. M.; Maggio, J. E.; Lee, J. P. *J. Struct. Biol.* **2000**, *130*, 130–141.
 (31) Bashford, D.; Gerwert, K. *J. Mol. Biol.* **1992**, *224*, 473–486.
 (32) Bashford, D. In *Scientific computing in object-oriented parallel environments*; Ishikawa, Y., Oldehoeft, R. R., Reyniers, J. V. W., Tholburn, M., Eds.; Springer: Berlin, 1997; Vol. 1343, pp 233–240.
 (33) Lipari, G.; Szabo, A. *J. Am. Chem. Soc.* **1982**, *104*, 4546–4559.
 (34) Kordel, J.; Skelton, N. J.; Akke, M.; Palmer, A. G., III; Chazin, W. J. *Biochemistry* **1992**, *31*, 4856–4866.

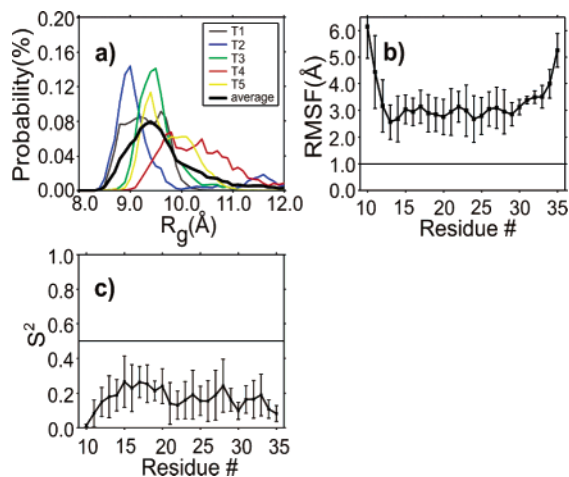


Figure 1. Measures of global structural fluctuations: (a) distribution of the radius of gyration for the five independent trajectories labeled T1, T2, T3, T4, and T5; (b) root-mean-square fluctuations (measured with respect to the initial conformation) of the backbone atoms; (c) Lipari–Szabo order parameter, S^2 .

3. Results and Discussion

3.1. Compact $A\beta_{10-35}$ Undergoes Large Structural Fluctuations. The distributions of the radius of gyration $P(R_g)$ for the five trajectories show substantial variations (Figure 1a) which may be indicative of the heterogeneity in the sampled conformations. If $A\beta_{10-35}$ adopts a compact conformation, as indicated in our previous study,³⁵ we expect the average value of $\langle R_g \rangle \approx aN^{1/3}$ with a between 3 and 3.8 Å. For the 26-residue peptide, $8.9 \text{ Å} < \langle R_g \rangle < 11.3 \text{ Å}$. We find from simulations that $\langle R_g \rangle = 9.7 \text{ Å}$, which shows that globally $A\beta_{10-35}$ is maximally compact. However, the distributions show large fluctuations as well (Figure 1a).

The residue-dependent root-mean-square (RMS) fluctuation of the backbone atoms is a measure of the stability of the peptide during MD simulations. In agreement with the results of an experimental structural determination of the $A\beta_{10-35}$ -protein in aqueous solution,³⁰ a previous simulation study by Massi et al.³⁵ showed, using a relatively short MD simulation, that $A\beta_{10-35}$ in a TIP3P solvent has a stable hydrophobic LVFFA(17–21) core and a VGSN(24–27) β -turn while the amino and carboxy termini are largely disordered. In the present work we find, using larger simulation times, that the core 13–29 is more stable than the termini (Figure 1b). Relative to the previous study, we find that there is a modest increase in the RMS fluctuations of the core. Thus, globularity in the monomeric $A\beta_{10-35}$ -protein might result as a consequence of the formation of the VGSN turn.

The Lipari–Szabo order parameter, S^2 , is used to characterize the extent of orientational fluctuations in the peptide backbone–amide bond vector. We had shown previously³⁵ that there is good agreement between computed and experimentally derived values of S^2 . Analyzing the corresponding S^2 values calculated from the present larger simulations (Figure 1c), we observe that, like in the previous study,³⁵ the hydrophobic core LVFF(17–20) is more stable relative to the rest of the peptide, with S^2 values between 0.2 and 0.3. Lower S^2 values are calculated for the E22 and D23 residues, 0.13 and 0.16, respectively, indicating their extended hydration. The ends of the VGSN(24–27) turn,

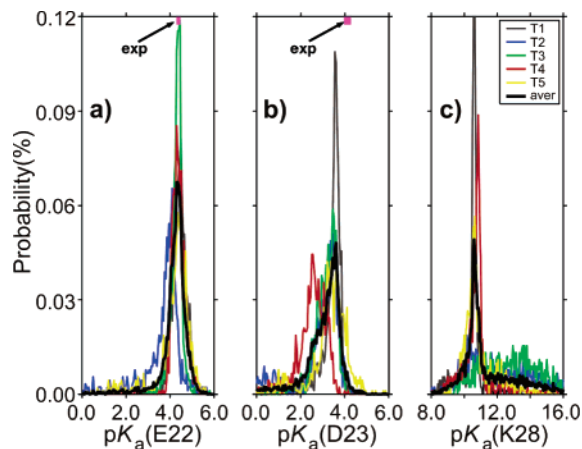


Figure 2. The distribution of the pK_a values indicates that E22, D23, and K28 are highly solvated in the $A\beta_{10-35}$ -protein. The D23 residue makes small favorable electrostatic interactions with the peptide. The small distribution in the positive pK_a shift for K28 indicates that the side chain of this residue tends to make a favorable electrostatic interaction with the rest of the $A\beta_{10-35}$ -protein. The experimental values were taken from ref 36.

the V24 and N27 residues, have larger S^2 values, both with 0.19, relative to the core of the turn, G25 and S26, both with 0.16. The N- and C-terminal regions of the $A\beta_{10-35}$ -protein have values of the S^2 order parameter of less than 0.2, in accordance with the increased flexibility of these regions (see Figure 1b). However, the small values of the S^2 order parameter, under 0.3, and the large values of the corresponding standard deviations indicate that the peptide samples a number of conformational basins during the course of the simulations. Higher values of S^2 are obtained over shorter simulation times. For example, we obtained values of S^2 larger than 0.6, calculated over a 1.0 ns time interval,³⁵ for the hydrophobic core LVFFA(17–21) and turn VGSN(24–27), defining basins with a compact hydrophobic core and a stable VGSN turn. However, the hydrophobic core is not large enough to reach stability over a longer simulation time. The electrostatic interactions between the charged ends of the VGSN(24–27) turn, E22, D23, and K28, are destabilized by their extended solvation.

3.2. Computed Values of pK_a Are in Accord with Experiments. We calculated the pK_a values of titratable residues of the $A\beta_{10-35}$ -protein and compared the results with the experimental values obtained using NMR titration³⁶ (see Figure 2). A critical parameter involved in this calculation, which influences the value of the electrostatic free energy of the partial charge distribution, is the relative dielectric constant of the protein interior, ϵ_i . Two ranges for the values of the protein interior dielectric constant are typically used. A value between 2 and 6 is used to represent the rigid structure of the protein,^{37–40} while a value between 20 and 36^{40–42} is used for the surface side chains to account for their larger fluctuations and associated dipole reorientation. Due to the moderate size of the $A\beta_{10-35}$ -protein, the central hydrophobic core LVFFA(17–21) is highly

(36) Zhang, S.; Lee, J. P. *J. Pept. Res.* **2000**, *55*, 1–6.

(37) Gilson, M. L.; Honig, B. H. *Biopolymers* **1986**, *25*, 2097–2119.

(38) Simonson, T.; Perahia, D.; Bricogne, G. *J. Mol. Biol.* **1991**, *218*, 859–886.

(39) Simonson, T.; Perahia, D.; Brunger, A. T. *Biophys. J.* **1991**, *59*, 670–690.

(40) Smith, P. E.; Brunne, R. M.; Mark, A. E.; Van Gunsteren, W. F. *J. Phys. Chem.* **1993**, *97*, 2009–2014.

(41) King, G.; Lee, F. S.; Warshel, A. J. *Chem. Phys.* **1991**, *95*, 4366–4377.

(42) Simonson, T.; Perahia, D. *Proc. Natl. Acad. Sci. U.S.A.* **1995**, *92*, 1082–1086.

(35) Massi, F.; Peng, J. W.; Lee, J. P.; Straub, J. E. *Biophys. J.* **2001**, *80*, 31–44.

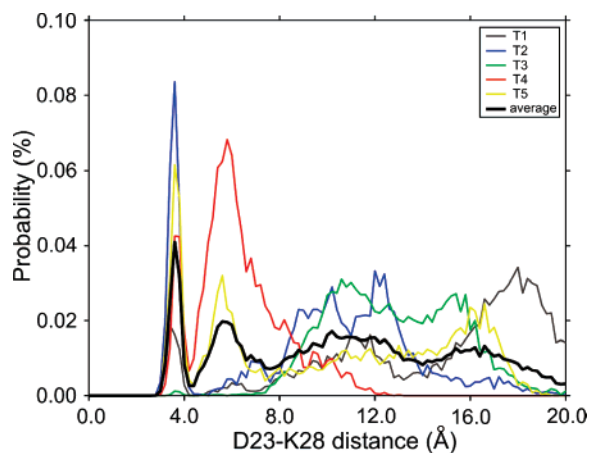


Figure 3. Distributions of the distance between the C_{γ} (D23) and N_{ζ} (K28) atoms as a measure of the salt-bridge D23–K28 stability. There are substantial sample-to-sample variations, which are indicative of the dynamic heterogeneity of the monomer.

exposed to solvent, making it difficult to define a rigid interior with a fixed low dielectric constant ϵ_i . We used two values for ϵ_i , 4 and 20, and compared the predicted pK_a values. In the TIP3P solvent model, the pK_a differences corresponding to the two ϵ_i values are less than 0.35 unit for E22, D23, and K28. As shown in Figure 3, the forms of charged D23 and K28 do not form a stable salt bridge, implying that D23 and K28 do not influence the dielectric constant ϵ_i of the peptide.

Both D23 and K28 residues are predominantly in their ionized forms³⁰ in the solvated $A\beta_{10-35}$ -protein at pH 7. It appears that, even in the fibril state of $A\beta_{1-40}$, D23 and K28 are ionized. As a result, these residues interact to form a crucial intramolecular salt bridge, thus satisfying the PASA. The averaged pK_a values, which are listed in Table 1, correlate well with the experimental values. There is good agreement between simulations and experiments for E22, while for H13, H14, and D23 the pK_a values are lower in the MD simulations. This indicates that our simulations capture a subensemble in which H13, H14, and D23 have a propensity to form favorable intrapeptide electrostatic interactions.

The distributions of computed pK_a values for E22, D23, and K28 are shown in Figure 2. For residue E22, both the predicted and experimental pK_a values are close to the model's pK_a value, indicating that the E22 residue is solvated, in good agreement with prior NMR experimental³⁰ and theoretical³⁵ observations. Residues D23 and K28 have favorable deprotonation and protonation tails, respectively. This suggests a tendency for favorable intrapeptide electrostatic interaction in a subset of the simulated ensemble of structures (see below).

3.3. Structures with an Intact D23–K28 Salt Bridge Are Not the Most Stable. The structure of the $A\beta_{10-35}$ -protein monomer, determined using NMR, shows evidence for the formation of the salt bridge D23–K28 in an aqueous environment.³⁰ There is also experimental^{16,43} and theoretical⁴⁴ evidence that this salt bridge is involved in oligomer stability and in the process of fibril formation of the amyloid β -protein. We find that, in the early stages, the salt bridge D23–K28 is partially buried in the interior of the $A\beta_{10-35}$ -protein and is stable during

the first nanosecond of the simulation in the explicit solvent (data not shown). However, due to the dielectric screening and the hydrogen bonds between the side chains of D23 and K28 and the water molecules within the first solvation shell, the salt bridge D23–K28 is subsequently disrupted. The distance distribution in Figure 3 shows that only a small fraction among the ensemble of conformations form the D23–K28 salt bridge. There is a broad distribution of compact structures stabilized by a variety of intramolecular interactions.

Two snapshots of the $A\beta_{10-35}$ -protein, in which the D23–K28 salt bridge is absent (Figure 4a,b), show that the two side chains are separated by three and two solvation shells, respectively. Clearly, a stable intramolecular salt bridge can only form if the interning water molecules can be expelled. This involves overcoming a large desolvation barrier.

The larger separation observed in Figure 4a is determined by the interposed side chain of V24 between D23 and K28. This results in a hydrophobic contact between V24 and the aliphatic portion of the K28 side chain. This hydrophobic contact was observed within the decapeptide $A\beta_{21-30}$ through experimental NMR studies by Lazo et al.⁴⁵ and in MD simulations.⁴⁶ We observe that F20 is buried in the peptide (Figure 4a), making hydrophobic contacts with both V24 and the butyl portion of the K28 side chain. The competition between the electrostatic D23–K28 and the hydrophobic V24–K28 interactions stabilizes the turn in the region V24–N27. A stable turn in the 24–27 domain also favors hydrophobic contacts between the hydrophobic core 17–21 and the C-terminus. This point is borne out in parts a and b of Figure 4, which show contacts between L17 and V18, on one hand, and I31 and I32, on the other hand. Contacts between the hydrophobic domain 17–21 and C-terminus are also observed in models of fibrils made of $A\beta_{10-35}$ ¹⁵ and $A\beta_{1-40}$.⁶ An increase of the distance between V24 and K28 favors the contact between D23 and K28. Figure 4c shows a D23–K28 water-mediated salt-bridge structure in which one water molecule makes hydrogen bonds with both the D23 and K28 side chains. Because the $A\beta_{10-35}$ -protein monomer is isolated in aqueous solution, large-scale conformational fluctuations are likely, which render the contacts mentioned above only marginally stable.

3.4. Multiple Basins Are Populated in the $A\beta_{10-35}$ Monomer. Figure 1a shows that the $A\beta_{10-35}$ monomer samples structures with extended values of the radius of gyration R_g . The probability of observing large R_g values (larger than 12 Å) is very low, but nonzero. In the T1–T4 trajectories, the structure of the $A\beta_{10-35}$ -protein shows large fluctuations in the end-to-end distance. In contrast, trajectory T5 is characterized by transitory stability of the hydrophobic core LVFFA(17–21) and turn VGSN(24–27). Moreover, hydrophobic interactions between the LVFFA(17–21) and C-terminal regions supplement the stability of the VGSN(24–27) turn. Consequently, as T5 shows multiple transitions (Figure 3) between the stable and broken D23–K28 salt bridge, we extended the simulation time of T5 to 60 ns. The stability of the contact between the D23 and K28 residues was characterized in terms of the free energies associated with the structural states in which the two residues are in contact or separated. The free energy associated with the

(43) Petkova, A. T.; Leapman, R. D.; Guo, Z.; Yau, W. M.; Mattson, M. P.; Tycko, R. *Science* **2005**, *307*, 262–265.

(44) Ma, B.; Nussinov, R. *Proc. Natl. Acad. Sci. U.S.A.* **2002**, *99*, 14126–14131.

(45) Lazo, N. D.; Grant, M. A.; Condrón, M. C.; Rigby, A. C.; Teplow, D. B. *Protein Sci.* **2005**, *14*, 1581–1596.

(46) Borreguero, J. M.; Urbanc, B.; Lazo, N. D.; Buldyrev, S. V.; Teplow, D. B.; Stanley, H. E. *Proc. Natl. Acad. Sci. U.S.A.* **2005**, *102*, 6015–6020.

Table 1. Experimental and Predicted pK_a Values (Using the Trajectories Labeled T1–T5) for Titratable Residues in the $A\beta_{10-35}$ -Protein^a

residue	exptl value ³⁶	T1	T2	T3	T4	T5
H13	6.11 ± 0.10	4.94 ± 0.59	5.48 ± 0.63	4.64 ± 1.27	2.36 ± 1.81	4.51 ± 1.75
H14	6.10 ± 0.10	4.30 ± 1.85	5.25 ± 0.77	3.11 ± 2.05	5.33 ± 1.00	2.93 ± 3.64
E22	4.38 ± 0.09	4.43 ± 0.31	3.60 ± 1.06	4.30 ± 0.30	4.37 ± 0.31	4.15 ± 0.60
D23	4.12 ± 0.16	3.44 ± 0.43	2.82 ± 1.10	3.13 ± 0.56	2.33 ± 1.02	3.27 ± 0.89
K28	na	10.44 ± 0.89	12.36 ± 2.29	12.82 ± 1.72	10.80 ± 1.00	11.67 ± 1.50

^a The predicted pK_a values are for $A\beta_{10-35}$ -protein structures simulated in the explicit solvent model TIP3P. A value of $\epsilon_1 = 4$ was used as the protein dielectric constant.

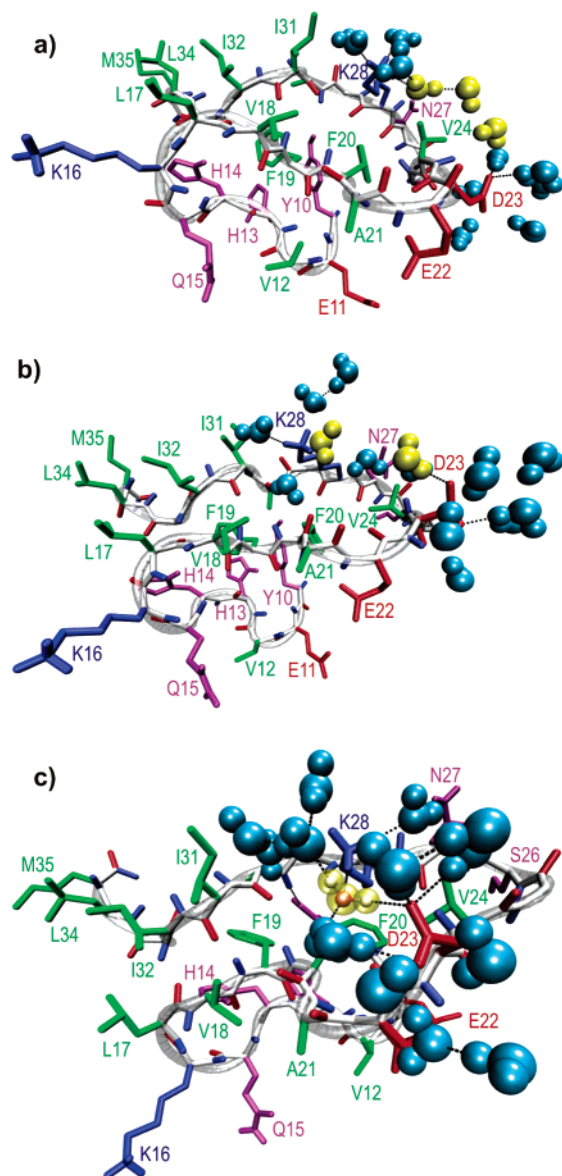


Figure 4. The hydrophobic interaction between V24 and the aliphatic portion of K28 leads to a large separation between D23 and K28, three solvation shells in (a). A decrease of the contact between V24 and K28 reduces the distance between D23 and K28 to two solvation shells (b) and less than one solvation shell (c). The backbone oxygen and nitrogen atoms are colored in red and blue, respectively. The positively charged, polar, and hydrophobic residues are colored in blue, red, purple, and green, respectively. Water molecules around D23 and K28 are colored in cyan, while water molecules which separate the two residues are shown in yellow. Hydrogen bonds are shown as black dashed lines. The figure was made by using VMD⁶² and rendered with POV-Ray.⁶³

transition between the formed and disrupted D23–K28 salt bridge was also evaluated. We considered that the D23 and K28 residues are in contact whenever there is less than a solvation

shell between the acetate and methylammonium groups of the two residues, respectively. This definition of the D23–K28 contacts allows us to consider not only the hydrogen-bonded D23–K28 contacts, which do not form frequently, but also weak, solvated D23–K28 electrostatic contacts.

An important parameter that characterizes the formation of the D23–K28 salt bridge encapsulated within the interior of the peptide is the degree of solvent exposure of the two residues. We considered residues D23 and K28 to be buried if the solvent-exposed surface area of the acetate or methylammonium groups is less than 5% of the total area. According to this definition, residue D23 is always solvated during the simulation, which is in accordance with the observation that the pK_a shift for D23 is rarely an unfavorable positive value (see Figure 2b). In contrast, the solvent exposure of the residue K28 reveals that it is either solvated or buried in the peptide interior, in accordance with the pK_a shift, which is either positive or negative (see Figure 2c).

The free energy is expressed as⁴⁷

$$F_{ij} = -k_B T \ln(N_{ij}) \quad (1)$$

where $i = j$ corresponds to the free energy of state i , while $i \neq j$ corresponds to the free energy of transition between states i and j . N_{ii} is the number of microstates in basin i , and N_{ij} is the number of transitions between basins i and j . The maximum number of transitions between basins i and j was obtained using the Gomory–Hu “minimum cut” algorithm.⁴⁸ The definitions of the four superbasins (combinations of the D23–K28 electrostatic contact and the burial of the D23 and K28 side chains in the peptide interior) include a diverse set of peptide structures. For example, a peptide structure might have a stable D23–K28 salt bridge but fluctuating N- and C-terminal regions. The maximum value of the radius of gyration R_g in the T5 trajectory, is limited to 11 Å during the 60 ns simulation, suggesting that the sampling of the major intrapeptide contacts, responsible for the peptide stability, is carried out at equilibrium. We can assume that the microstates in the four basins and the transitions among them are in equilibrium. A more detailed analysis of the substates within each basin, obtained from root-mean-square displacements of the backbone atoms of less than 2 Å, for example, would require a longer simulation time to sufficiently populate the substates and obtain a satisfactory number of transitions among them, which would ensure the desired macroscopic equilibrium. We have used a coarse-grained clustering algorithm based on the contacts between the residues D23 and K28 and the degree of exposure to solvent of these two residues.

(47) Krivov, S. V.; Karplus, M. *J. Chem. Phys.* **2002**, *117*, 10894–10903.

(48) Gomory, R. E.; Hu, T. C. *J. Soc. Ind. Appl. Math.* **1961**, *9*, 551–570.

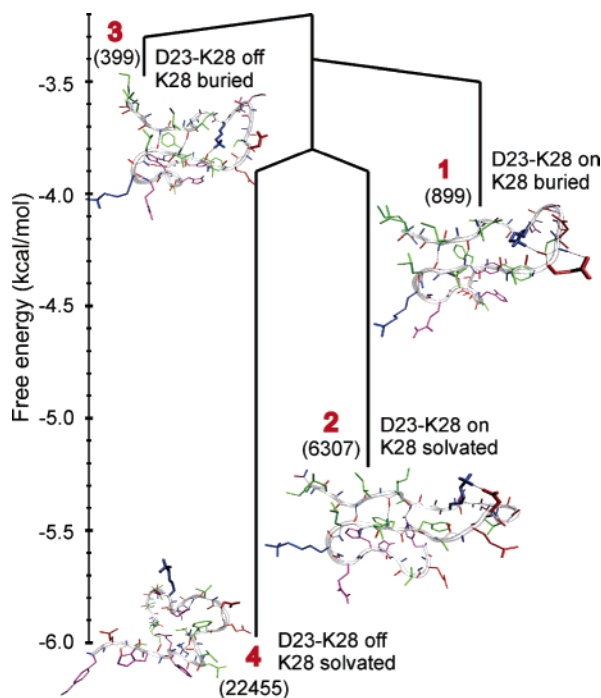


Figure 5. The process of formation and disruption of the D23–K28 salt bridge is represented as a free energy disconnectivity graph. Two superbasins characterize the states with the D23–K28 salt bridge formed or broken. Two possible conformations of the residue K28, solvated or buried, are represented as subbasins. The disrupted salt bridge is the more favorable state, and a large barrier makes the transition between the formed and disrupted substates improbable. Burying K28 in the peptide interior is an unfavorable process. The number of microstates associated with each of the four basins is indicated in parentheses. “D23–K28 on” stands for salt bridge present, while “D23–K28 off” stands for salt bridge broken.

Figure 5 shows a free energy disconnectivity graph^{47,49,50} used to represent the process governing the formation and disruption of the D23–K28 salt bridge in the $A\beta_{10-35}$ -protein. Possible intermediate states were analyzed by dividing the two superbasins corresponding to the D23–K28 salt bridge being on and off into two subbasins, associated with K28 being solvated or buried in the peptide interior. Since D23 is largely solvated during the simulation, its contribution to the energetics of the D23–K28 salt bridge was not represented as an essential degree of freedom in the graph.

We used 3×10^4 structures, recorded every 2 ps, to obtain the graph in Figure 5. In 75% of the structures, the D23–K28 salt bridge is broken. Figure 5 shows that the basin corresponding to fully solvated K28 with no salt bridge is the most probable state during the simulation, with 22455 realizations, corresponding to a free energy of -6.0 kcal/mol (basin 4). The broken D23–K28 salt bridge buries the K28 side chain in only 399 states (-3.5 kcal/mol, basin 3). A transition-state barrier of -3.2 kcal/mol separates the two possible substates of the broken salt bridge. During the simulations, the salt bridge is observed in 7206 ($\sim 25\%$) structures. The solvated salt bridge (basin 2) is the predominant stable salt bridge substate, with a free energy of -5.2 kcal/mol, while the salt bridge with K28 buried (basin 1) corresponds to a free energy of -4.1 kcal/mol. The two substates are separated by a transition barrier of -3.4 kcal/mol. A total of 739 transitions were observed between the formed and broken salt bridge basins.

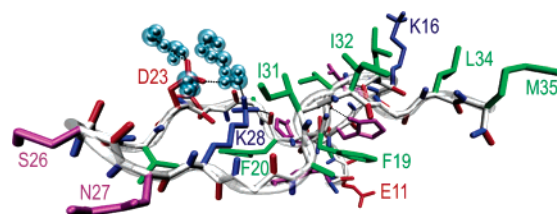


Figure 6. Structure indicating that the side chain of the K28 residue is buried in the interior of the peptide. The electrostatic interactions between the ammonium group of K28, on one side, and the backbone carbonyl oxygen atoms of F20 and E22 and the side chain carboxylate of D23, on the other side, are supplemented by the hydrophobic interaction between the aliphatic part of the K28 side chain and the side chains of V24 and I31. The same color scheme as in Figure 4 was used.

A free energy of 0.3 kcal/mol is necessary to form the salt bridge once the K28 side chain is buried in the peptide interior. A free energy of 0.9 kcal/mol is required to disrupt the salt bridge, keeping the K28 side chain buried. These observations demonstrate that the D23–K28 salt bridge is only marginally stable at room temperature. From Figure 5 we surmise that the buried K28 in the salt bridge is more stable (899 microstates) than the buried K28 in the broken salt bridge (399 microstates). The difference is given by the favorable contribution to the salt bridge stability of the hydrophobic interaction between the aliphatic part of the K28 side chain and the side chains of V24 and I31. A representative structure is shown in Figure 6. These results are in agreement with the conclusions in experimental NMR studies and molecular dynamics simulations that the hydrophobic interaction between V24 and the aliphatic part of the K28 side chain stabilizes the VGSN (24–27) turn in the fragment $A\beta_{21-30}$.^{45,46} However, to bury the K28 side chain is an energetically expensive operation. The cost to bury the salt bridge is 1.8 kcal/mol, while the cost to bury K28 in the broken salt bridge is 2.7 kcal/mol. The difference of 0.9 kcal/mol between these two states further rationalizes the experimental observation that a lactam bond between D23 and K28 accelerates the fibril formation process.⁵¹ Our simulations show that the bottleneck in the formation of a stable, buried D23–K28 pair is the burial of the K28 residue.

The equilibrium distribution of distances between the C_α atoms of the V24 and N27 residues provides insight into the stability of the VGSN(24–27) fragment (see Figure 7). It can be observed that the VGSN(24–27) fragment samples two domains. The burial of K28 and the interaction between the hydrophobic part of the K28 side chain and V24 stabilizes a single-turn conformation, characterized by values of the C_α –($V24$)– C_α (N27) distance between 6 and 7.5 Å. Importantly, this conformation allows close interaction between the central hydrophobic core LVFFA(17–21) and the hydrophobic C-terminus (domain I in Figure 7). The flexibility of the backbone around G25 allows the side chain of V24 to rotate and form an alternative loop with G25 and D23, while GSNK(25–28) forms an additional proximate loop. Consequently, the distance C_α –($V24$)– C_α (N27) increases to 8.3 – 10.0 Å (domain II in Figure 7), and the hydrophobic contact between the C-terminus and the LVFFA(17–21) fragment is reduced. The bimodal behavior of the 23–28 domain provides a possible explanation for the increased flexibility of the $A\beta_{10-35}$ -protein (see Figure 1a,b).

(49) Czerminski, R.; Elber, R. *J. Chem. Phys.* **1990**, *92*, 5580–5601.
 (50) Evans, D. A.; Wales, D. J. *J. Chem. Phys.* **2003**, *118*, 3891–3897.

(51) Sciarretta, K. L.; Gordon, D. J.; Petkova, A. T.; Tycko, R.; Meredith, S. C. *Biochemistry* **2005**, *44*, 6003–6014.

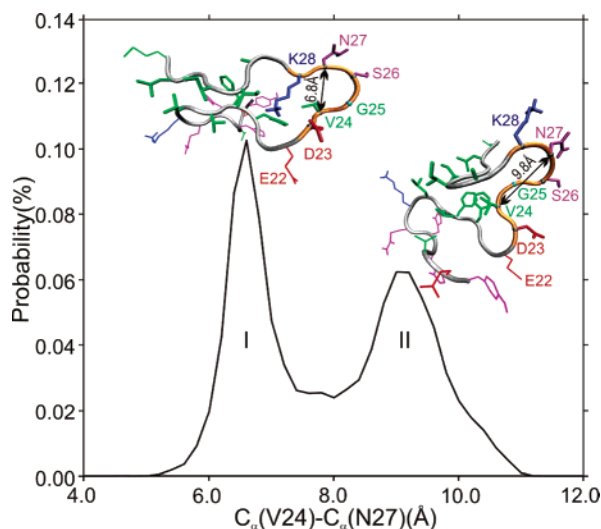


Figure 7. The distribution of the $C_{\alpha}(V24)-C_{\alpha}(N27)$ distance reveals the dual character of the 23–28 fragment stability. A low value of the $C_{\alpha}(V24)-C_{\alpha}(N27)$ distance allows for hydrophobic interaction between the LVFFA(17–21) central hydrophobic cluster and the C-terminus of the peptide. The same color scheme as in Figure 4 was used.

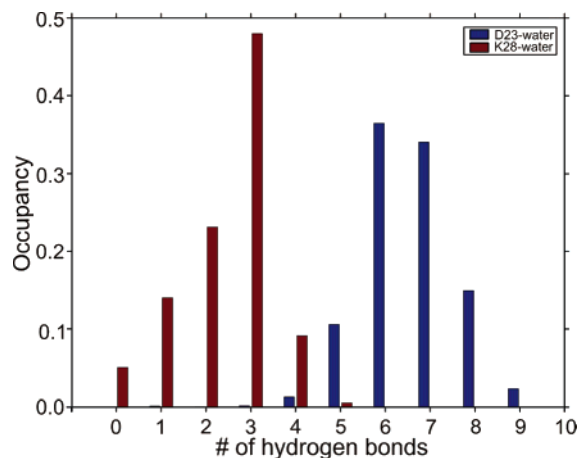


Figure 8. The distribution of the hydrogen bonds reveals that the D23 side chain is highly solvated during the entire period of simulation while the K28 side chain can make transient hydrogen bonds with the peptide backbone.

3.5. Hydrogen Bonds with Water Increase the Desolvation Barrier of D23 and K28. The dynamics of the hydrogen bonds between water and the side chains of D23 and K28 was analyzed during the trajectory T5. A hydrogen bond is considered formed if the distance between the hydrogen atom of the donor and acceptor is shorter than or equal to 2.5 Å and the D–H...A angle is higher than 113°. The distribution of the number of hydrogen bonds made by D23 and K28 side chains with water is shown in Figure 8. The carboxylate group of D23 is highly solvated and forms 6.6 hydrogen bonds with water on average. Coincidentally, a totally solvent-exposed aspartate side chain also makes approximately the same number of hydrogen bonds with water. The ammonium group of K28 makes, on average, 2.4 hydrogen bonds with water, less than 3.3 corresponding to a lysine side chain that is fully exposed to water. The decrease in the number of hydrogen bonds between the K28 ammonium

group and water is compensated by the hydrogen bonds made by K28 mostly with the peptide backbone (see Figure 6).

The lifetimes of the hydrogen bonds between the D23 and K28 side chains and water were also computed and compared to the lifetime of the hydrogen bonds in bulk water. To avoid the trivial breaking of the hydrogen bonds due to librational motion, we considered that the hydrogen bonds are stable if their lifetimes exceed 0.2 ps.⁵³ A lifetime of 0.9 ps for the hydrogen bonds in the bulk water was found, in good agreement with ~0.8 ps obtained from interpretation of depolarized Rayleigh scattering spectra.⁵⁴ We estimated the lifetimes of the hydrogen bonds made by the fully solvated charged side chains of D23 and K28 with water. The lifetime of the oxygen δ acceptors made by D23 was found to be 2.5 ps, while that for the hydrogen ζ donors of K28 was 2.3 ps. We conclude that the side chains of D23 and K28 make stronger contacts with water than water with itself, indicating that the desolvation of D23 and K28 is an activated process. In addition, we also find that D23 makes more contacts with water than K28, which explains the stronger solvation of D23 compared to K28.

3.6. Burial of K28 Involves a Large Free Energy Cost.

To rationalize the low probability of forming the electrostatically stabilized D23–K28 salt bridge, we have computed the free energy cost of burying the side chain of K28 in the peptide interior using

$$\Delta G_{\text{bur}} = \Delta G_{\text{desolv}} + \Delta G_{\text{inter}} + \gamma \Delta S_{\text{SAS}} \quad (2)$$

where ΔG_{desolv} is the desolvation free energy and ΔG_{inter} is the free energy of the electrostatic interaction between the side chain and the peptide interior. The favorable decrease of the solvent volume displaced by the side chain is proportional to the decrease in surface exposed to the solvent, ΔS_{SAS} . By solving the Poisson equation, we estimated a desolvation free energy cost of 68.2 kcal/mol to remove the lysine side chain from a highly polar solvent ($\epsilon_i = 80$) to a vacuum ($\epsilon_i = 1$). However, in our case, the side chain of K28 is not placed into a vacuum; it is in a low-dielectric environment of the solvated peptide. Consequently, the high free energy cost to bury the K28 side chain in an extended vacuum is dramatically reduced when the K28 side chain is buried with $\Delta G_{\text{desolv}} = 13.8 \pm 3.2$ kcal/mol. Once buried, the side chain of K28 makes favorable electrostatic interactions, in the form of hydrogen bonds between the nitrogen ammonium of K28 and the carbonyl oxygen atoms of the backbone peptide. We estimated the free energy to be $\Delta G_{\text{inter}} = -6.9 \pm 3.6$ kcal/mol. With an average surface area of 200.6 Å² buried by the K28 side chain, and a value between 20 and 30 cal/(mol Å²) for γ , it seems to be quite close to the value of the free energy difference between basins 4 and 1 or 4 and 3 in Figure 5. Using these estimates, we surmise that $\Delta G_{\text{bur}} \approx 7$ kcal/mol, which is very steep indeed. It should be mentioned that, in the estimate of ΔG_{bur} , the unfavorable reduction of entropy due to the interaction between the K28 side chain and the peptide interior was not considered. Thus, our estimate of ΔG_{bur} is likely to be a lower bound.

3.7. Structure of Water around Residues D23 and K28.

The pair radial distribution function (RDF) was used to analyze the structure of water around residues D23 and K28 in trajectory

(52) Simmerling, C.; Elber, R.; Zhang, J. In *Modelling of biomolecular structure and mechanisms*; Pullman, A., Jortner, J., Pulman, B., Eds.; Kluwer: Dordrecht, The Netherlands, 1995; pp 241–265.

(53) Luzar, A.; Chandler, D. *Nature (London)* **1996**, *379*, 55–57.

(54) Montrose, C. J.; Bucaro, J. A.; Marshall-Coakley, J.; Litovitz, T. A. *J. Chem. Phys.* **1987**, *60*, 5025–5029.

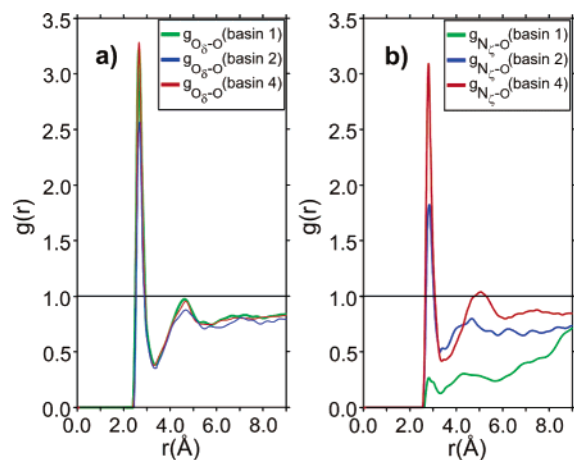


Figure 9. Discrete water molecules play a substantially different structural role that depends on the peptide basin. The structure of water around D23 and K28 is analyzed in terms of radial distribution functions between the pairs of the O_{δ} (D23) and N_{ζ} (K28) atoms with the water oxygen atoms. The fully solvated D23 and K28 side chains, characterizing the conformations in basin 4, have on average 3.7 water molecules in the first solvation shell around the O_{δ} (D23) and N_{ζ} (K28) atoms. Once the D23 and K28 side chains are in electrostatic contact, but still solvated (basin 2), the number of water molecules decreases to 3.0 and 2.7 around the O_{δ} (D23) and N_{ζ} (K28) atoms, respectively. In basin 4, burying the K28 side chain in the peptide interior is possible after its desolvation, while the weak electrostatic contact between the D23 and K28 side chains allows the O_{δ} atoms to maintain the waters forming the first solvation shell.

T5. Figure 9 shows the averaged pair radial distribution function between the oxygen δ atoms of D23 and the water oxygen atoms (a) and between the nitrogen ζ atom of K28 and the water oxygen atoms (b). The RDF profiles displayed in both (a) and (b) correspond to $A\beta_{10-35}$ -protein conformations in which the D23–K28 contact buries the K28 side chain in the peptide interior (basin 1 in Figure 5), the D23–K28 contact is solvated (basin 2), and the D23 and K28 side chains are separated and fully solvated (basin 4). The first solvation shells around the O_{δ} (D23) and N_{ζ} (K28) lie between 2.4 and 3.3 Å and between 2.6 and 3.3 Å, respectively. The large exposure of D23 and K28 to solvent in basin 4 corresponds to a maximum of the RDF profiles in the first solvation shell. From the area under the graph, an average of 3.7 water molecules was found to form the first solvation shell surrounding the O_{δ} (D23) and N_{ζ} (K28) atoms in the lowest free energy structure in basin 4. In basin 2, where the contact between the acetate of D23 and the methylammonium of K28 is solvated, less water is observed in the first solvation shells, O_{δ} (D23) and N_{ζ} (K28) atoms losing 0.6 and 0.9 water molecule, respectively.

There is a dramatic decrease in the water density in the proximity of N_{ζ} (K28) in the structures in basin 1. On average, we find about 0.5 water molecule, since the side chain of K28 is buried in the peptide interior (see Figure 9b, green curve). Somewhat surprisingly, the RDF profile of the water molecules around the O_{δ} (D23) atoms in basin 1 (green curve in Figure 9a) is practically identical to the profile in basin 4. It appears that the O_{δ} (D23) atoms keep the water expelled between the acetate group of D23 and the methylammonium group of K28. By burying its side chain in the interior of the peptide, K28 makes hydrogen bonds with the backbone of the peptide. As a consequence, the contact between D23 and K28 in basin 1 is maintained by the electrostatic interaction between their opposite charges, and not by a hydrogen bond. This results in a fluctuating contact, with the O_{δ} (D23) atoms free to maintain

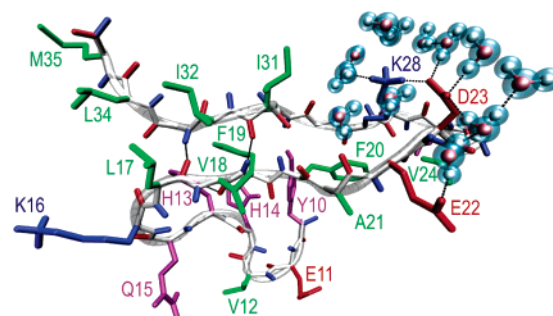


Figure 10. The D23–K28 salt bridge and hydrophobic interactions keep the fragments 17–21 and 30–34 in contact. The same color scheme as in Figure 4 was used.

favorable contacts with solvating waters. The structure of water in basin 3, where the D23 side chain is fully solvated and the K28 side chain buried in the peptide interior, with no significant electrostatic interaction between them, is similar to the structure of water around O_{δ} (D23) in basin 4 and around N_{ζ} (K28) in basin 1, respectively (data not shown).

4. Summary and Conclusions

Given the importance of the intramolecular^{6,7} and intermolecular⁹ salt bridge D23–K28 in the $A\beta_{1-40}$ amyloid fibrils, we probed its structure and stability in the monomeric protein using all-atom MD simulations in explicit water. The primary motivation for this study is to assess whether the salt bridge is preformed in the monomer. We found that the $A\beta_{10-35}$ -protein fluctuates among a number of conformational substates. During the course of the simulations, the anionic D23 residue is solvated. The cationic K28 residue was found to be both solvated and buried in the peptide interior. The electrostatic interaction between D23 and K28 contributes to the conformational stability of the β -turn VGSN(24–27), an important structural motif in the experimentally observed NMR structure.³⁰ The VGSN turn also plays a crucial role in facilitating the formation of the bend in the monomer. The bend is necessary in facilitating the parallel architecture of long $A\beta$ -proteins. We estimate a small favorable electrostatic interaction of -0.34 kcal/mol.

In the most solvated conformations of the D23 and K28 side chains, basin 4, their O_{δ} (D23) and N_{ζ} (K28) atoms are surrounded on average by 3.7 water molecules in the first solvation shells. When the D23 and K28 side chains are still solvated but in contact, ranging from weak, solvated electrostatic interaction to a stronger hydrogen bond, the carboxylate oxygen and the ammonium nitrogen atoms lose on average 0.6 and 0.9 water molecule from the first solvation shells, respectively (basin 2). A more exposed K28 in basin 2 can form hydrogen-bonded contacts with the D23 side chain acceptors (Figure 10). Comparison of the structure of the isolated $A\beta_{10-35}$ monomer with an intact D23–K28 contact and the conformations that $A\beta_{1-40}$ ^{6,7} and $A\beta_{1-42}$ ⁹ adopt in the quaternary structures of putative fibril models reveals the extent of conformational fluctuations required in the formation of the fibril from protein monomers. In both fibril models, the 17–26 and 30–40 fragments are in β -strand conformations, forming two parallel β -sheets whose faces are linked by intersheet hydrophobic interactions. In the $A\beta_{1-40}$ ^{6,7} fibril structure, the D23–K28 salt bridge is intramolecular, while in $A\beta_{1-42}$ ⁹ the D23–K28 salt bridge is intermolecular. There are arguments that the D23–K28 salt bridge plays an important role in the fibril stability in

both models.^{6,7,9} The main similarity of our MD simulation results with the proposed fibril structures^{6,7,9} is that the bend in the region 23–28 causes the fragments 17–21 and 30–34 to adopt an antiparallel orientation. This orientation is further stabilized by hydrophobic interactions between L17 and I32, L17 and L34, V18 and I31, and F19 and A30. In the $A\beta_{1-42}$ ⁹ fibril structure, the intersheet hydrophobic contacts are made between the residues F19 and G38 and A21 and V36. The reduced hydrophobic contacts are explained by the rigidity of the monomers within the fibril structure of $A\beta_{1-42}$ ⁹. To maximize the contact surface between the hydrophobic residues in our MD simulations, they are not within the intrapeptide plane defined by the strands 17–21 and 30–34 as in $A\beta_{1-40}$ ^{6,7} or the interpeptide plane defined by the strands 17–26 and 30–41 as in the $A\beta_{1-42}$ ⁹ fibril structure. In the MD simulation of the isolated $A\beta_{10-35}$, the hydrophobic contacts are perpendicular to these planes. Consequently, the distance between the backbones of the 17–21 and 30–34 strands is smaller in the $A\beta_{10-35}$ monomer, which makes it possible to form hydrogen bonds (O(L17)–N(G33) and N(F19)–O(I31)) (Figure 10). In the fibril structures of $A\beta_{1-40}$ ^{6,7} and $A\beta_{1-42}$ ⁹ the hydrophobic contacts are maximized by interdigitation of the hydrophobic side chain interactions. In the fibril structure of $A\beta_{1-42}$ ⁹ the 17–26 strand has its backbone hydrogen bond donors and acceptors participating in a β -sheet with neighboring monomers. In contrast, the isolated $A\beta_{10-35}$ monomer has unfulfilled hydrogen bond donors and acceptors in the more sterically accessible 17–21 region. The 10–15 region reduces the solvent-exposed surface by making a bend around K16 and contacts with the 17–21 region through a hydrogen bond, N δ_1 (H14)–O(V18), and hydrophobic contacts between the phenol rings of Y10 and F19 and F20 (Figure 10). The comparison illustrates the dramatic interpeptide-interaction-driven conformational changes in the cascade of events from monomers to fibrils.

The burying of the K28 side chain in the peptide interior, observed in basin 1, implies its desolvation. The stability of the buried K28 side chain is attributed to the formation of hydrogen bonds between its N ζ atom and the carbonyl oxygen atoms of the peptide backbone. As a consequence, the ability of the K28 side chain to form hydrogen bonds with the D23 side chain is strongly diminished. The contact in basin 1 is maintained by weak, solvent-screened electrostatic interactions between the opposite charges of the D23 and K28 side chains, with the O δ (D23) atoms remaining largely solvated.

The fact that the D23–K28 salt bridge is observed in the monomer in a minority of structures which could result in a structural motif that can nucleate and grow can be most directly linked to the high desolvation cost of burying charges, especially D23 and K28. It follows that the conformational fluctuations in the monomers that create a stable D23–K28 interaction in the fibril must occur due to interpeptide interactions. Interactions between peptides can only occur if the peptide concentration C_P exceeds a minimum threshold. At high values of C_P the conformational fluctuations of a given monomer are restricted due to volume excluded by neighboring monomers. As a result, the monomer is forced to adopt conformations in a “crowded” environment. It is likely that the equilibrium between the substates could shift as C_P increases. Our simulations show that salt bridge formation with a stable VGSN turn can only form when C_P is increased so that interpeptide interactions become

relevant. The coupling between interpeptide interactions and forces that stabilize the monomers will determine the conformations of the $A\beta$ -proteins as the transitions to fibrils occur via oligomers and protofilaments.

A related question concerns the significance of specific weak interactions in protein aggregation. The heterogeneity observed in oligomers and the disorder characteristic of amyloid fibrils is a result of structural stabilization through a variety of weak and somewhat disordered hydrophobic contacts. In the peptide studied, the D23–K28 salt bridge is found to provide a mild stabilization of the VGSN turn, which is an important structural motif observed in simulations of the peptide monomer and present in fibrils formed by the $A\beta_{1-40}$ -protein.^{6,7} It is puzzling that such weak stabilizing interactions are sufficient to produce stable ordered fibrils in relatively short times. Indeed, similar arguments have been in the context of folding of globular proteins. To rationalize rapid folding of proteins, it was shown that a slight energetic bias in favor of nativelike conformations at the residue level leads to substantial reduction in the time for folding.⁵⁵ Similarly, it is likely that several weak stabilizing interactions, such as that associated with the D23–K28 salt bridge formation, are sufficient in the nucleation of monomer structures consistent with the growth of the fibril state.

The results of our simulations also provide insight into the nature of denatured states in proteins at neutral pH. A number of experimental studies^{56,57} on globular proteins at nonzero concentrations of denaturants suggest that there is considerable structure present in the unfolded states. The $A\beta$ -protein is disordered in the absence of denaturants and can be considered as being intrinsically disordered. The disconnectivity graph clearly shows that the ensemble of unfolded states can be partitioned into a cluster of four dominant substates. Within each substate there is evidence for rapidly interconverting fluctuating structures. In addition, transitions between structures within each basin are rapid, whereas interbasin transitions involve crossing a free energy barrier. It is possible that similar structural considerations apply to denaturant-induced unfolded states of globular proteins. If this is indeed the case, then the heterogeneity of folding is a consequence of the imprint of the various substates that are sampled in the ensemble of unfolded states. It will be interesting to enumerate the disconnectivity graphs for unfolded globular proteins to assess their impact on folding kinetics.

A major conclusion of this work is that discrete water molecules, which solvate charges and facilitate hydrogen bond formation, play a key role in preventing the formation of the D23–K28 salt bridge in the monomer. We have found that this picture of the conformational fluctuations in the monomer is not captured if continuum electrostatics ACE^{58,59} and GBORN⁶⁰ and solvent-exclusion EEF1⁶¹ implicit solvent models are used.

- (55) Zwanzig, R.; Szabo, A.; Bagchi, B. *Proc. Natl. Acad. Sci. U.S.A.* **1992**, *89*, 20–22.
 (56) Shortle, D.; Ackerman, M. S. *Science* **2001**, *293*, 487–489.
 (57) Klein-Seetharaman, J.; Oikawa, M.; Grimshaw, S. B.; Wirmer, J.; Duchardt, E.; Ueda, T.; Imoto, T.; Smith, L. J.; Dobson, C. M.; Schwalbe, H. *Science* **2002**, *295*, 1719–1722.
 (58) Schaefer, M.; Karplus, M. *J. Phys. Chem.* **1996**, *100*, 1578–1599.
 (59) Schaefer, M.; Bartels, C.; Karplus, M. *J. Mol. Biol.* **1998**, *284*, 835–848.
 (60) Dominy, B. N.; Brooks, C. L., III. *J. Phys. Chem. B* **1999**, *103*, 3765–3773.
 (61) Lazaridis, T.; Karplus, M. *Proteins: Struct., Funct., Genet.* **1999**, *35*, 133–152.
 (62) Humphrey, W.; Dalke, A.; Schulten, K. *J. Mol. Graphics* **1996**, *14*, 33–38.
 (63) <http://www.povray.org>.

Moreover, the use of an implicit solvent fails to reproduce experimentally measured pK_a values of the titratable groups (B. Tarus, J. E. Straub, and D. Thirumalai, unpublished work). It appears that a molecular description of the early events in the oligomerization of $A\beta$ -proteins requires explicit inclusion of water molecules.

Acknowledgment. B.T. thanks Dr. Naoyuki Miyashita for stimulating discussions about the computational estimation of pK_a in proteins. We thank Dr. Nicolae-Viorel Buchete for helpful

discussions about the structure of $A\beta$ fibrils. This work was supported by a grant from the National Institutes of Health (R01 GM076688-05).

Supporting Information Available: Complete ref 24. This material is available free of charge via the Internet at <http://pubs.acs.org>.

JA064872Y